Micron-scale pattern formation in prestressed polygonal films

Annabattula, R. K.; Onck, P. R.

Published in:
Journal of Applied Physics

DOI:
10.1063/1.3544467

Publication date:
2011

Micron-scale pattern formation in prestressed polygonal films

R. K. Annabattula and P. R. Onck[a)]
Zernike Institute for Advanced Materials, University of Groningen, Nijenborgh 4, 9747 AG Groningen, The Netherlands

(Received 27 September 2010; accepted 11 December 2010; published online 11 February 2011)

In this paper we explore the spontaneous formation of micropatterns in thin prestressed polygonal films using finite element simulations. We study films with different size, thickness, and shape, including square, rectangular, pentagonal, and hexagonal films. Patterns form when the films release the internal eigenstrain by buckling-up, after which the films bond-back to the substrate. After an initial symmetric evolution of the buckling profile, the symmetry of the deflection pattern breaks when the wavelength of wriggles near the film edges decreases. During bond back the deflection morphology converges to a fourfold, fivefold, and sixfold ridging pattern for the square, pentagonal and hexagonal films, respectively, showing a close resemblance with experimental film systems of similar size and shape. Rectangular films of large length to width ratio go through a transition in buckling shapes from the initial Euler mode, through the varicose mode into the antisymmetric telephone-cord mode. For all the film shapes, the ratio of the film height to the effective film width scales with the square root of eigenstrain and is independent of thickness. The bond-back mechanism determines the final wrinkle morphology and is governed by the eigenstrain value at the end of the buckling-up stage and the dimensionless parameter $(\Gamma/EW_{eq})(W_{eq}/t)^3$, relating the interface energy to the strain energy in the film. © *2011 American Institute of Physics*.
[doi:10.1063/1.3544467]

I. INTRODUCTION

Wrinkled surfaces are omnipresent in many systems in nature such as vegetables, fruits, leaves, and human skin. Such patterns/wrinkles of thin surfaces with controllable dimensions at the micrometer and nanometer scale are promising tools for modern technological applications as, e.g., microelectromechanical systems (MEMS). In recent times it has been successfully demonstrated that these patterned surfaces can be used as tunable optical gratings,[1–3] replica for microfluidic channels,[4] flexible electronics,[5–9] microfluidic channels,[10,11] microreactors,[12] particle separators,[13] tissue engineering applications,[14] surfaces for marine antifouling,[15] devices for DNA manipulation,[16,17] and templates for microstructure fabrication.[18,19]

While nature controls the shape and size of patterns observed in natural systems (vegetables, leaves, etc.) through complex biochemical processes along with mechanical forces, the microsystems mentioned above need sophisticated processes to be developed for better control and reproducibility. In the last two decades, there was considerable effort to develop fabrication methods and the most successful of them are based on the three-step process of conventional lithography, thin film deposition, and etching.[20–24] However, these lithography based methods are time consuming and they become expensive as the feature size reduces. In the search for alternatives a method based on the self-organization of surface patterns and channels through the buckling of prestressed thin films was found to be promising for it does not require prepatterning at small length scales.[25] Since then, thin film buckling has been explored in a wide range of applications[26–29] describing how the—otherwise unwanted—phenomenon of buckling could be used to develop MEMS and nanomechanical systems for various technological applications.

Recently, it has been demonstrated that an additional level of complexity can be introduced based on the release and bond-back of prestressed thin films,[4,10,11] leading to patterns with different morphologies (Fig. 1). Figures 1(a) and 1(b) show optical micrographs of fourfold and fivefold ridge patterns on square and pentagonal films formed by pulse electrolysis proposed by Edmondson and Huck.[3] In their method, thin polymer polyglicydylmethacrylate (PGMA) brushes are grown and cross-linked on a gold substrate. Then, the film-substrate system is placed in an electrolytic cell and a short electric pulse is given to break the bonds between the film and the substrate, resulting in buckling-driven relaxation of the prestressed polymer film followed by bond-back. The final pattern morphology depends strongly on the film shape (lines, square, pentagons, etc., see Edmondson *et al.*[4]). Figures 1(c) and 1(d) show scanning electron microscope (SEM) images of a nanochannel network fabricated by Malachias *et al.*,[11] based on the same mechanism of release, buckling-up, and bond-back. In their method semiconductor films are epitaxially grown on sacrificial-layer-covered substrates. For a square pattern of circular etch pits a diagonal buckling pattern develops [Figs. 1(c) and 1(d)] that shows a clear resemblance with the fourfold ridging pattern for the square polymer films [Fig. 1(a)]. The objective of this paper is to understand the mechanics of pattern formation in these prestressed thin film systems and study how the film geometry (thickness, size, and shape) and film and interface properties (prestrain, stiffness, and interface energy) relate to the final pattern morphology. To do so, we will

[a)]Electronic mail: p.r.onck@rug.nl.

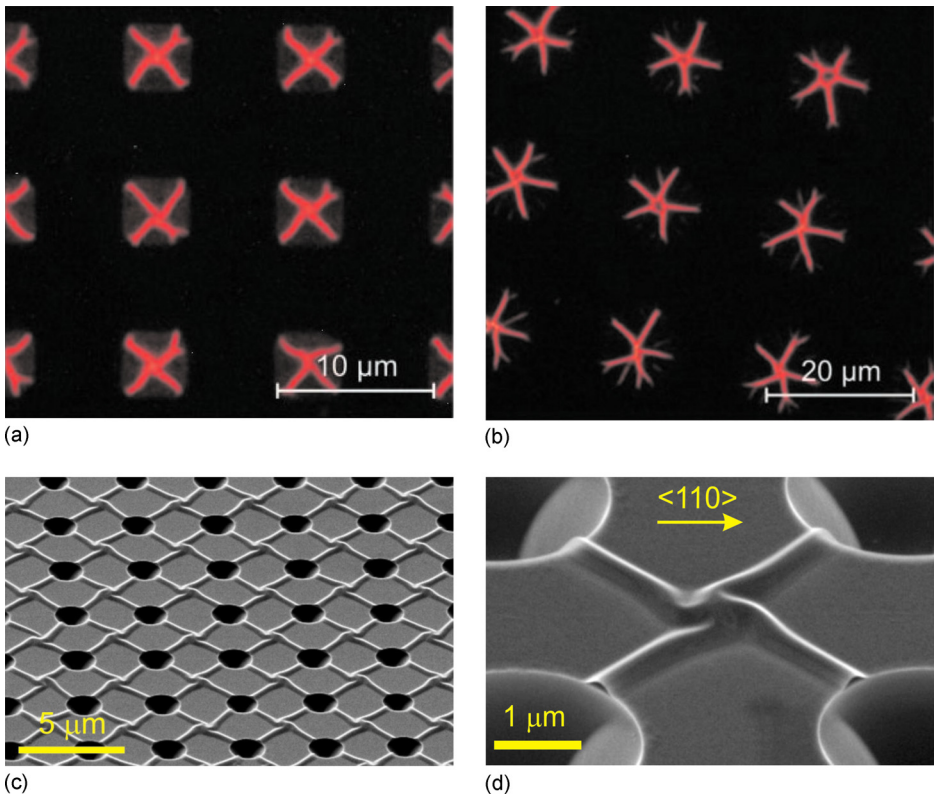

FIG. 1. (Color online) Patterns formed by the release and bond back of prestressed thin films. [(a) and (b)] Optical micrographs of fourfold and fivefold ridge patterns formed in square (a) and pentagonal (b) polymer films released by pulse electrolysis (reproduced with permission from Edmondson *et al.* (Ref. 4)]. (c) SEM image of a nanochannel network formed by the controlled underetching of semiconductor films [reproduced with permission from Malachias *et al.* (Ref. 11)]. (d) A zoomed view of one unit-cell of (c).

perform three-dimensional (3D) finite element calculations to simulate the buckling, postbuckling, and bond back of prestressed thin film systems following closely the experimental set up of Edmondson *et al.*[4]

The paper is organized as follows. In Sec. II the boundary value problem is described followed by a detailed discussion of the numerical ingredients. In Sec. III we present the results of our simulations, in which we subsequently analyze buckling-up and bond back of square (Sec. III A), rectangular (Sec. III B), pentagonal and hexagonal films (Sec. III C). Finally, in Sec. IV, we summarize and conclude the article.

II. PROBLEM DEFINITION AND METHOD

In this section, we define the mechanical boundary value problem to describe the above mentioned mechanism for pattern formation. Figure 2 shows the schematic of various stages in the process: (i) film growth, during which the film is prestrained with an eigenstrain ε^* [Fig. 2(a)]; (ii) release of eigenstrains by buckling of the film into a domelike shape due to reduction in interface strength between film and substrate [Fig. 2(b)], and (iii) bond-back of the buckled-up film (due to cohesive interaction between the film and the substrate) forming a final ridge shape [Fig. 2(c)]. In the present

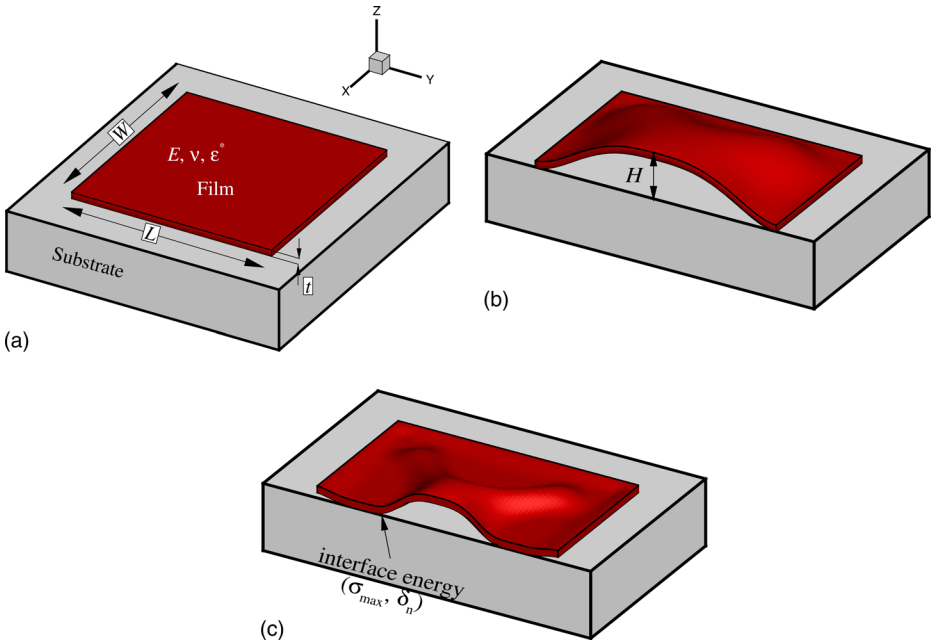

FIG. 2. (Color online) Schematic of the pattern formation mechanism (a) initial stage, (b) buckled-up configuration, and (c) configuration after bond-back.

study we combine the first two steps by loading the film with eigenstrain in the absence of any interface cohesion. In doing so, we neglect all details connected to buckling-driven interface delamination due to the gradual reduction in interface strength, as studied in a two-dimensional setting by Annabattula *et al.*[30] In their study it was shown that the driving force for delamination at the edge of the film drastically reduces, so that full delamination only occurs in the presence of large eigenstrains. We incorporate this observation in the present analysis by simply constraining the edges of the film. We study a film of width W (and length L in case of rectangular films), thickness t, Young's modulus E, and Poisson's ratio ν on a rigid substrate. Also pentagonal and hexagonal films will be analyzed in Sec. III C, following the same approach as explained here for square and rectangular films.

Using von Karman nonlinear plate theory, the total strain in the film can be written as the sum of three contributions,[31]

$$\boldsymbol{\varepsilon} = \boldsymbol{\varepsilon}^{\mathrm{str}} + \boldsymbol{\varepsilon}^{\mathrm{rot}} + \boldsymbol{\varepsilon}^{\mathrm{bend}}. \tag{1}$$

The first term, $\boldsymbol{\varepsilon}^{\mathrm{str}}$, is the strain caused by the in-plane stretching of the material and its coefficients with respect to a Cartesian frame in the x-y plane [see Fig. 2(a)] are

$$\varepsilon_{ij}^{\mathrm{str}} = \frac{1}{2}\left(\frac{\partial u_i}{\partial x_j} + \frac{\partial u_j}{\partial x_i}\right), \quad i = 1,2, \ \ j = 1,2, \tag{2}$$

with u_i the in-plane displacements. The second term, $\boldsymbol{\varepsilon}^{\mathrm{rot}}$, is the contribution caused by the out-of-plane displacements w and is given by

$$\varepsilon_{ij}^{\mathrm{rot}} = \frac{1}{2}\frac{\partial w}{\partial x_i}\frac{\partial w}{\partial x_j}, \quad i = 1,2, \ \ j = 1,2. \tag{3}$$

The contribution of the strain caused by bending/curvature of the plate is given by

$$\varepsilon_{ij}^{\mathrm{bend}} = -z\frac{\partial^2 w}{\partial x_i \partial x_j} = -z\chi_{ij}, \quad i = 1,2, \ \ j = 1,2. \tag{4}$$

For the constitutive behavior of the film, we assume that the total strain consists of an elastic part $\boldsymbol{\varepsilon}^{\mathrm{el}}$ and an eigenstrain part $\boldsymbol{\varepsilon}^{\mathrm{eig}}$: $\boldsymbol{\varepsilon} = \boldsymbol{\varepsilon}^{\mathrm{el}} + \boldsymbol{\varepsilon}^{\mathrm{eig}}$, with the eigenstrain given by

$$\varepsilon_{ij}^{\mathrm{eig}} = \varepsilon^{*}\delta_{ij}, \quad i = 1,2, \ \ j = 1,2, \tag{5}$$

with δ_{ij} the Kronecker delta. The film is in a state of plane stress ($\sigma_{13} = \sigma_{23} = \sigma_{33} = 0$) so that the coefficients of the stress $\boldsymbol{\sigma}$ in the plate are given by

$$\sigma_{ij} = \frac{E}{1+\nu}\left(\varepsilon_{ij}^{\mathrm{el}} + \frac{\nu}{1-\nu}\varepsilon_{kk}^{\mathrm{el}}\delta_{ij}\right), \tag{6}$$

where $i = 1,2$, $j = 1,2$, E is Young's modulus, and ν is Poisson's ratio of the film. To mimic the complex interplay between the film and substrate during drying, we assume a phenomenological interaction relation that consists of a short-range repulsive part and a long-range attractive part, also often employed for van der Waals-type interactions. During bond-back the film experiences a vertical downward traction T_{n}, causing the normal separation w_{n} between the film and substrate to decrease. For this we use a nonlinear traction-separation relation given by Xu and Needleman[32]

$$T_{\mathrm{n}} = \sigma_{\max}\frac{w_{\mathrm{n}}}{\delta_{\mathrm{n}}}\exp\left(1 - \frac{w_{\mathrm{n}}}{\delta_{\mathrm{n}}}\right), \tag{7}$$

where $\sigma_{\max}$ is the maximum normal traction attained at the critical normal opening δ_{n}. The cohesive energy per unit area is equal to $\Gamma = \int_{w_{\mathrm{n}}} T_{\mathrm{n}} dw_{\mathrm{n}} = \sigma_{\max}\delta_{\mathrm{n}}\exp(1)$.

III. RESULTS AND DISCUSSION

In this section, we analyze the strain-driven pattern evolution in films of different shapes, i.e., square, rectangular, pentagonal, and hexagonal films, followed by bond back. To solve the boundary value problem defined in Fig. 2 we use the finite-element method.[33] The film is discretized by four-noded shell elements (S4) (Ref. 34) with all boundaries of the film fully constrained and the substrate is modelled as a rigid surface (R3D4).[35] We assume that the material of the film is linear elastic with an elastic modulus $E = 7$ GPa and Poisson's ratio $\nu = 0.32$. To trigger buckling the initial configuration of the film is perturbed in the out-of-plane direction with sufficiently small imperfections. A static solution procedure is used during the buckling-up stage (eigenstrain loading) with a stabilization procedure to overcome small local instabilities.[34] The maximum allowable dissipated energy due to stabilization is limited to 3% of the total strain energy of the film. The bond-back stage is carried out using an explicit dynamic solution procedure so that the inertia of the film can be used to overcome local instabilities; the loading rate however is kept small to mimic quasi-static loading. We also incorporate a "no-separation" contact condition with rough friction during bond-back so that the nodes of the film that come in contact with the substrate will effectively be anchored from that instant onwards. Furthermore, we use a mass-proportional damping (Rayleigh damping) during bond-back, such that the total energy dissipated is a small fraction (5%) of the total strain energy in the film. During bond-back the film is acted upon by a nonuniformly distributed normal traction based on the cohesive interface law proposed by Xu and Needleman,[32] as given in Eq. (7). It has been shown previously[36] that the final bond-back configuration is fully governed by the interface energy $\Gamma = \sigma_{\max}\delta_{\mathrm{n}}\exp(1)$, while the individual values of $\sigma_{\max}$ and δ_{n} do not have a significant influence. Hence, in this work we use $\delta_{\mathrm{n}} = 20$ nm and increase the interface energy Γ through $\sigma_{\max}$ in the bond-back simulations.

A. Square films

In this section, we study various aspects of the pattern evolution during eigenstrain loading followed by bond-back in square films. The film thickness t and film size W will be varied in the range of 20–50 nm and 2–5 μm, respectively. Figure 3 shows the results for a square film of size 5 μm and thickness 30 nm (reference case). The top row shows the pattern evolution during the buckling-up stage and the bottom row shows the bond-back stage. The contour plots correspond to the vertical position z of the film (see Fig. 2). During eigenstrain loading, the film accommodates the strain by in-plane compression. When the eigenstrain reaches a critical strain, the film buckles. The critical buckling-load P_{cr}

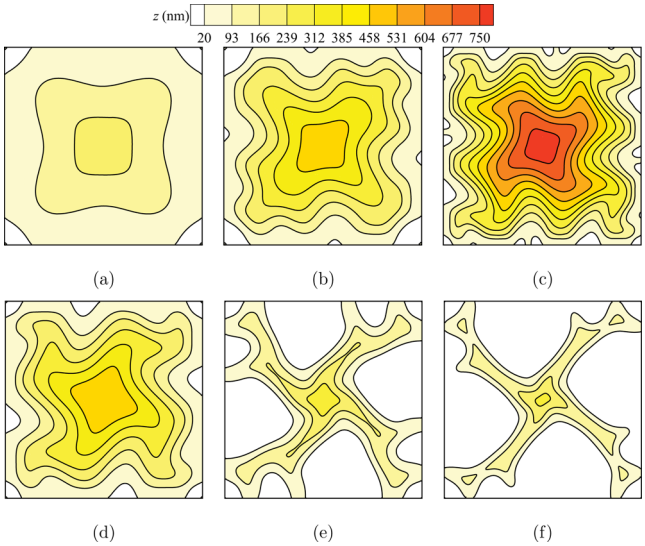

FIG. 3. (Color online) Evolution of deflection patterns of a square film of width $W=5$ μm and thickness $t=30$ nm during the buckling-up [(a)–(c)] and bond-back stages [(d)–(f)]. The bond-back process is started from the configuration at 1.9% eigenstrain (d). (a) $\varepsilon^*=0.3\%$, (b) $\varepsilon^*=1.78\%$, and (c) $\varepsilon^*=5.0\%$. The normalized interface strength (σ_{max}/E) during bond back is (d) 0.0, (e) 0.3×10^{-3}, and (f) 0.5×10^{-3}.

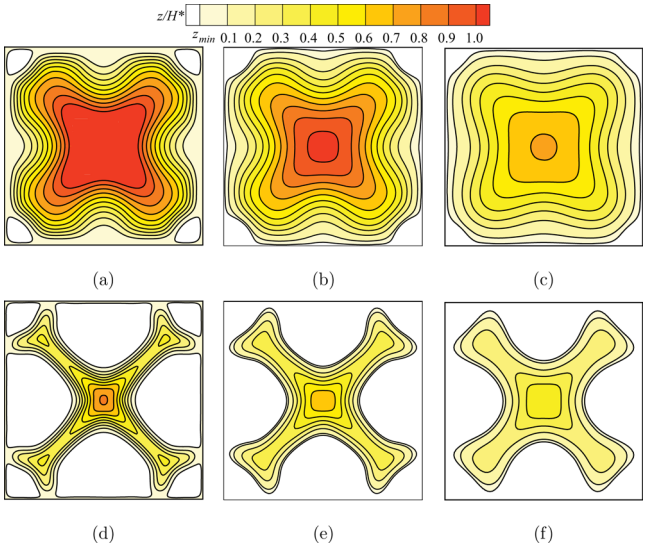

FIG. 4. (Color online) Evolution of deflection patterns during bond-back of square films of thickness 30 nm but for different size [(a) and (d)] $W=4$ μm, [(b) and (e)] $W=3$ μm, [(c) and (f)] $W=2$ μm. The first row corresponds to the initial configuration of the bond back (i.e., at 2% eigenstrain). The second row corresponds to a value of $\sigma_{max}/E=0.5\times10^{-3}$. The contours show the out-of-plane position of the film (z) normalized with $H^*=300$ nm and $z_{min}=20$ nm/H^* for all the cases shown in this article.

for square films clamped along the edges has been obtained using analytical techniques[37,38] and is given by

$$P_{cr}=5.3\frac{D\pi^2}{W^2}, \tag{8}$$

with $D=Et^3/12(1-\nu^2)$. By using $\sigma_{cr}=P_{cr}/t$ and $\varepsilon^*_{cr}=\sigma_{cr}(1-\nu)/E$ it follows that

$$\varepsilon^*_{cr}=\frac{5.3\pi^2}{12(1+\nu)}\left(\frac{t}{W}\right)^2. \tag{9}$$

Figure 3(a) shows the out-of-plane displacement of the film at 0.3% eigenstrain after initial buckling, which happened at $\varepsilon^*_{cr}\approx0.011\%$, with a similar buckling profile as in Fig. 3(a). It can be observed that the profile is symmetric with respect to a horizontal and vertical axes through the center. At a certain strain level the symmetry is broken, associated with a reduction in wavelength near the boundary, which further decreases with strain [see Figs. 3(b) and 3(c)]. Figure 3(d) shows the profile at the beginning of the bond-back process at 1.9% eigenstrain. When the interface strength is increased the film starts to bond back at the center of the four edges [Fig. 3(e)], ultimately "freezing" in a diagonal ridge pattern [Fig. 3(f)]. It can be observed that the final pattern evolved after bond back has a very close resemblance with the experimentally-obtained patterns shown in Fig. 1(a).

Figure 4 shows the contour plots of the out-of-plane deflection during the bond-back stage for $W=4$ μm (first column), 3 μm (second column), and 2 μm (third column) for a film thickness $t=30$ nm. The contour plots in the first row correspond to the configuration at the beginning of the bond-back process (i.e., at the end of 2% eigenstrain during buckling-up). The contour plots in the second row are shown at $\sigma_{max}/E=0.5\times10^{-3}$, the final point of the bond-back simulation. Note that the configuration at 2% strain is symmetric for all widths. It turns out that for $W=4$ and 3 μm, the onset of symmetry breaking during buckling-up stage (results not shown) occurs right after 2% (at 2.1%) and for $W=2$ μm at 4.7%. Clearly, when the film width reduces, the breaking of symmetry is postponed to larger strain values. As a result, during bond back the system is stable, yielding regular square patterns.

Figure 5(a) shows the evolution of buckling amplitude H as a function of normalized eigenstrain $\bar{\varepsilon}^*$ during buckling-up (left hand frame) and as a function of σ_{max}/E during bond-back (right hand frame) for films of size $W=2$, 3, 4, and 5 μm with a film thickness of 30 nm. The normalized eigenstrain $\bar{\varepsilon}^*$ is the ratio of eigen strain ε^* to the maximum eigenstrain applied which is 1.9% for $W=5$ μm film and 2% for remaining cases. As mentioned before, the buckling-up configuration at 2% eigenstrain (with an exception of 1.9% for 5 μm film) is the starting point for the bond-back simulation. Clearly, the buckling height H increases with increasing film size W, during both stages of the process (buckling-up and bond-back). Next, we take films of size $W=5$ μm and change the film thickness [$t=20$, 30, and 40 nm, see Fig. 5(b)]. The buckling amplitude during the buckling-up stage appears to be independent of the thickness. During bond-back, however, the effect of the film thickness on the final height can be clearly seen, leading to increasing buckle heights with increasing thickness. Figure 6 shows the corresponding deflection patterns during the bond-back stage for films of thickness 20 nm (first column), 30 nm (second column), and 40 nm (third column). The first row shows the buckled-up configuration at 2% eigenstrain [1.9% for Fig. 6(b)], which is the initial configuration for the bond-back process. Although the buckling amplitude H for all cases is approximately the same [see Fig. 5(b)], the effect of thickness comes in through the breaking of symmetry triggered by a reduction in wavelength near the edges [see Figs.

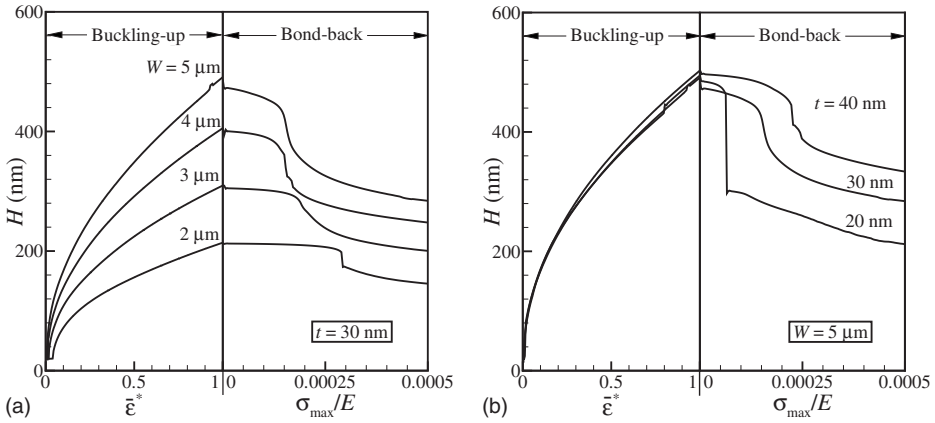

FIG. 5. Buckling height H at the central node during buckling-up as a function of normalized eigenstrain $\bar{\varepsilon}^*$ (left frame) and during bond-back as a function of σ_{max}/E (right frame) for films of widths 5, 4, 3, and 2 μm for a film thickness of 30 nm (a) and for a film width of 5 μm for different film thicknesses of 20, 30, and 40 nm (b).

6(a)–6(c)]. Only for $t=40$ nm the buckling-up process retains symmetry of film shape, while for the smaller thicknesses, the breaking of symmetry during buckling up causes a rotational asymmetry of the final bond-back configuration, characteristic for the patterns found in square films [see Figs. 6(d), 6(e), and 1]. For thicker films the rotation is not observed, thus resulting in a regular (nonrotated) fourfold pattern [see Fig. 6(f)]. There are two characteristic features in Figs. 6(d) and 6(e) that are also observed in the experimental systems shown in Fig. 1: (i) the splitting of the microchannels in the corners of the square films [see the upper right corner of the square films in Fig. 1(a)] and (ii) the breaking of symmetry leading to a rotated configuration of the fourfold ridging patterns [see Fig. 1(a)]. Clearly, the morphology of the final draped-back configuration depends on the onset of symmetry breaking during buckling up. The onset of asymmetry can be traced back to the buckling profile near the edges. In Fig. 7(a) we plot the out-of-plane (z) displacement along the length of the film [see X-X in Fig. 6(a)] for a film of thickness 20 nm at a distance of $W/8$ from the top boundary. The profile is plotted at different eigenstrain values, showing a clear decrease in wavelength with an increase in eigenstrain, during which the profile changes from a double sinusoidal shape ($\varepsilon^*=0.3\%$) to a more complex wriggling profile. The simulations show that the breaking of symmetry happens much sooner (i.e., at smaller eigenstrains) for thinner films and that the wavelength is larger (but the amplitude smaller) for thicker films for a given eigenstrain.

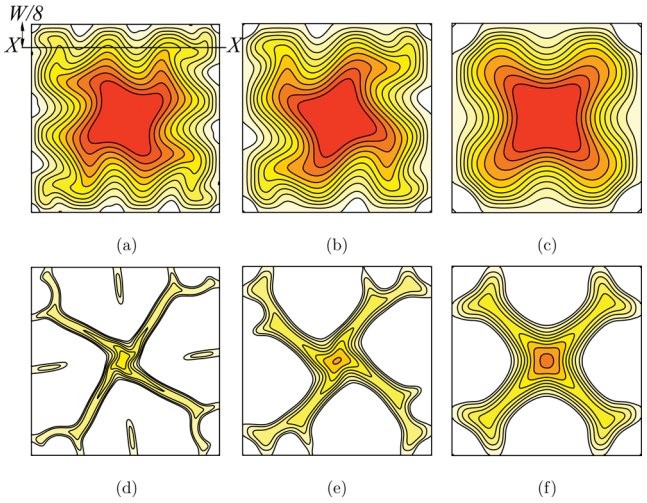

FIG. 6. (Color online) Evolution of deflection patterns of square films during the bond-back stage for different thicknesses. All the films are of size $W=5$ μm. The figures (a) and (d) correspond to film of thickness $t=20$ nm, [(b) and (e)] 30 nm, and [(c) and (f)] 40 nm, respectively. The first row corresponds to the configuration at 2% eigenstrain [1.9% for figure (b)] at the end of the buckling-up stages. The second row corresponds to a value of $\sigma_{max}/E=0.5\times10^{-3}$. The out-of-plane deflection z is normalized with $H^*=400$ nm. The contours have the same legend as Fig. 4.

To quantify this, we plot the normalized wavelength (λ_{ts}/W), i.e., the inverse of the number of waves, at the top strip (along X-X) as a function of eigenstrain in Fig. 7(b). The jumps in wavelength are discrete as the change in wavelength occurs at distinct eigenstrains due to mode-jumping in the postbuckling regime.[39] The trends that we observe here are similar to those found for linear nanochannel networks, showing a decrease in wavelength with strain, with wavelengths being larger for thicker films.[36] Figure 7(b) shows that the reduction in wavelength sets in at large eigenstrains when the film is thicker relative to its width. To explore this further, we plot the onset-strain ε^*_λ (i.e., the strain at which the buckling profile changes from being symmetric to asymmetric) as a function of normalized film thickness t/W in the inset of Fig. 7(b). Similar to the buckling strain this onset strain has an approximate square dependence on the slenderness t/W, see Eq. (9).

B. Rectangular films

In this section we investigate the evolution of the film deflection with an increase in eigenstrain for rectangular films. Figure 8 shows the contour plots of the out-of-plane (z) deflection of a rectangular film of length $L=5$ μm, width $W=2$ μm, and thickness $t=30$ nm [see Fig. 2(a)]. During the eigenstrain loading, we can observe that the film goes through three stages. Figure 8(a) shows the initial buckling mode, referred to as the Euler buckling mode. With further increase in eigenstrain, the film enters the varicose mode [Fig. 8(b)] and finally symmetry is broken when entering into a telephone-cord mode [Figs. 8(c)–8(f)]. A similar evolution of buckling modes with film stress in films of infinite length has also been reported by Moon *et al.*[29]

Figure 9 shows the contour plots of the out-of-plane deflection of rectangular films of length $L=5$ μm and widths $W=2$, 3.5, and 4.5 μm with a thickness $t=30$ nm, through the entire process of channel formation. The first column in

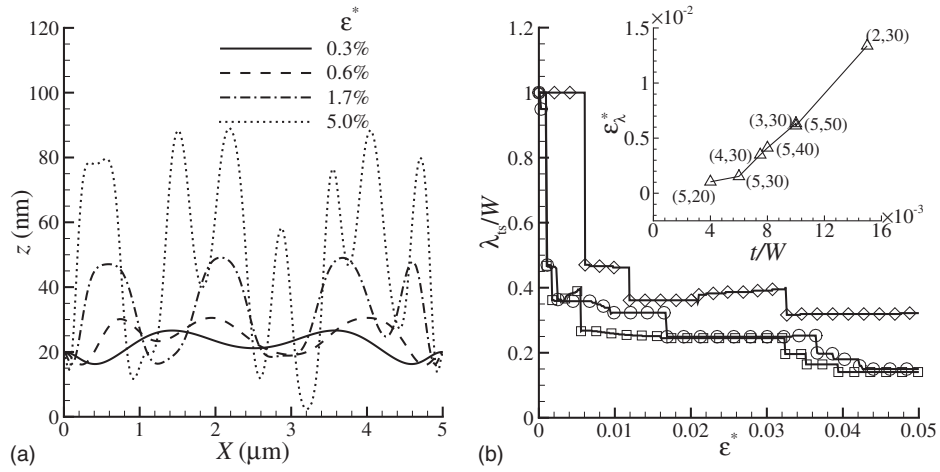

FIG. 7. (a) Out-of-plane deflection (z) of the film along the section (X-X) shown in Fig. 6(a) for a film of width $W=5$ μm and thickness $t=20$ nm at different eigenstrain values. (b) Normalized wavelength (λ_{ts}/W) at the top cut-section X-X as a function of eigenstrain ε^*. The symbols in figure (b) corresponds to different thickness and width combinations. Square symbols correspond to $W=5$ μm, $t=20$ nm, diamonds correspond to $W=3$ μm, $t=30$ nm and circles correspond to $W=2.5$ μm and $t=10$ nm. Inset of figure (b) shows the strain (ε^*_λ) at the onset of change in wavelength along X-X as a function of normalized film thickness (t/W). The numbers shown in parentheses of the inset of figure (b) represent (W,t), with W in micrometer and t in nanometer.

all the figures correspond to the initial buckled-up profile at small eigenstrain ($\varepsilon^*=0.19\%$), the second column corresponds to the fully buckled-up configuration at the end of eigenstrain loading (i.e., at 1.4% eigenstrain) and the third column corresponds to the configuration at the end of the bond-back process. It can be clearly seen that the final bond-back configuration strongly depends on the configuration at the beginning of bond-back; we see a nonsymmetric pattern formation for films of large length (L) to width (W) ratio and the pattern transforms to the well-known fourfold ridge pattern [Fig. 9(i)] for square films (see Sec. III A).

The switching of modes in the case of a confined rectangular film may be explained as follows. A prestressed rectangular film relaxes the stresses by buckling in the transverse direction (i.e., in the X-direction, see Fig. 2) at small strains, called the Euler mode. With further increase in strain the film starts to relax in the longitudinal direction (Y-direction) as well, resulting in a bifurcation of the Euler mode into a symmetric or antisymmetric undulating profile, termed varicose and telephone-cord mode, respectively. It has been shown by Audoly[40] that for an infinitely long rectangular film with a width W the bifurcation mode depends solely on Poisson's ratio of the film. If Poisson's ratio of the film is less than 0.25, the secondary mode will be symmetric (varicose mode) and if it is higher the mode will be antisymmetric (telephone-cord). In the case of a rectangular film of finite length and width the ratio of secondary buckling load to primary buckling load depends on the film aspect ratio and thickness. Indeed, our results show that for relatively large aspect-ratio films the Euler mode is followed by the varicose mode but that the telephone-cord mode is attained at relatively small eigenstrains (see Fig. 8). Increasing the aspect ratio, postpones the change from varicose to telephone-cord mode to larger eigenstrains, as shown in the second column of Fig. 9, where $W=2$ and 3.5 μm correspond to the telephone-cord mode, and $W=4.5$ μm to the varicose mode at 1.4% eigenstrain. Clearly, the buckling morphology (symmetric versus asymmetric) is directly reflected in the final configuration after bond-back (see right column of Fig. 9). Increasing the film thickness also postpones the varicose-to-telephone-cord bifurcation to larger strains (results not shown), also leading to more regular channel morphologies.

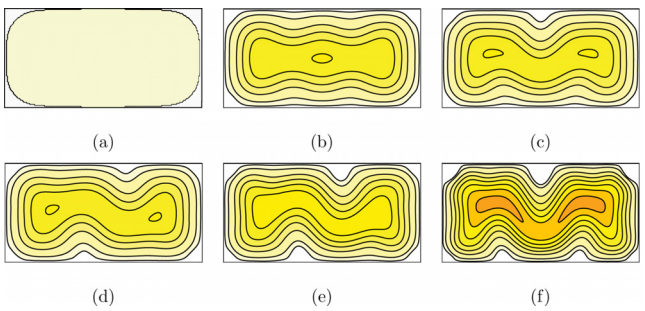

FIG. 8. (Color online) Evolution of deflection patterns during buckling-up for a rectangular film ($L=5$ μm, $W=2$ μm, $t=30$ nm). The contour plots correspond to eigenstrain ε^* of (a) 0.04%, (b) 0.53%, (c) 0.56%, (d) 0.57%, (e) 0.80%, and (f) 1.4%, respectively. The film subsequently buckles in the Euler mode (a), the varicose mode (b), and the telephone-cord mode (c). For the legend, see Fig. 4 with $z_{min}=0.067$ and $H^*=300$ nm.

We now investigate the evolution of the buckling height H as a function of eigenstrain for films of different length (L) to width (W) ratios. Figure 10(a) shows the evolution of the square of the normalized buckling amplitude (at the central node, i.e., at the intersection of the two diagonals) $(H/W)^2$ as a function of eigenstrain ε^* for films of different aspect ratio (i.e, for different widths W but for a fixed length $L=5$ μm and thickness $t=30$ nm). It can be observed that the effect of aspect ratio L/W on the normalized buckling amplitude H/W is very small. The sudden jumps in buckling amplitude (at $\varepsilon^*=0.005$, 0.0085 for $W=2$ μm and at $\varepsilon^*=0.012$ for $W=3.5$ μm) correspond to mode-changes (from Euler to varicose and from varicose to telephone-cord mode, see Figs. 8 and 9). The amplitude H reported in Fig. 10(a) corresponds to the central node, which was the highest node until the onset of mode change. When the mode change occurs, the highest point shifts and the amplitude of the central node

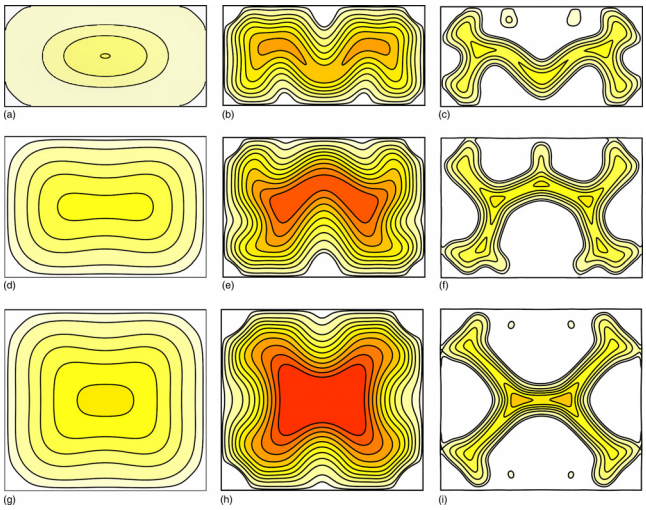

FIG. 9. (Color online) Evolution of normalized out-of-plane deflection during buckling-up and bond-back for rectangular films of thickness 30 nm, length $L=5$ μm, and width [(a)–(c)] $W=2$ μm, [(d)–(f)] $W=3.5$ μm, and [(g)–(h)] $W=4.5$ μm. The first column shows the initial buckling configurations at 0.19% eigenstrain, the second column corresponds to the final buckled-up configuration at 1.4% eigenstrain and the third column shows the final bond-back configuration (at $\sigma_{max}/E=0.142\times10^{-3}$). The out-of-plane deflection z is normalized with $H^*=300$ nm (see Fig. 4 for legend).

reduces. Next, we will develop an analytical solution to the postbuckling problem using minimization of energy.

The solution for the boundary value problem (for a rectangular film constrained all around) can be approximated by

$$w(x,y)=(H/4)[1-\cos(2\pi x/L)][1-\cos(2\pi y/W)], \quad (10)$$

where L and W are the length and width of the film, respectively (see Fig. 2). The membrane strain energy density (W_m) and bending strain energy density (W_b) are given by

$$W_m=\frac{t}{2}[\sigma_{11}\varepsilon_{11}^{el}+2\sigma_{12}\varepsilon_{12}^{el}+\sigma_{22}\varepsilon_{22}^{el}], \quad (11)$$

$$W_b=\frac{\bar{E}t^3}{24}\left[\left(\frac{\partial^2 w}{\partial x^2}\right)^2+\left(\frac{\partial^2 w}{\partial y^2}\right)^2+2\nu\frac{\partial^2 w}{\partial x^2}\frac{\partial^2 w}{\partial y^2}+2(1-\nu)\times\left(\frac{\partial^2 w}{\partial x\,\partial y}\right)^2\right], \quad (12)$$

with σ_{ij} defined in Eq. (6), $\bar{E}=E/(1-\nu^2)$ and the elastic strains in the film (neglecting the contribution due to axial displacements) given by (see also Sec. II)

$$\varepsilon_{ij}^{el}=-\varepsilon^*\delta_{ij}+\varepsilon_{ij}^{rot}. \quad (13)$$

The total bending (U_b) and membrane (U_m) strain energy are given by

$$U_b=\int_0^L\int_0^W W_b dxdy, \quad U_m=\int_0^L\int_0^W W_m dxdy, \quad (14)$$

and hence the total strain energy in the film is given by $U=U_b+U_m$. The amplitude of the film is obtained by minimizing the total strain energy

$$\frac{\partial U}{\partial H}(E,H,L,W,t,\nu,\varepsilon^*)=E\frac{\partial U^*}{\partial H}(H,L,W,t,\nu,\varepsilon^*)=0.$$

This results in an implicit equation for H, which can be solved for H and written as

$$\frac{H}{W}=f\left(\frac{t}{L},\frac{L}{W},\varepsilon^*,\nu\right). \quad (15)$$

It turns out that the analytical solution for H for films of fixed length L, width W as a function of ε^* shows a very small thickness dependence. Only for small strains a thickness-dependence can be observed (results not shown). A similar observation is also reported by Annabattula *et al.*[30] With the assumption that $t/L\ll\varepsilon^*$, Eq. (15) can be simplified to

$$\frac{H}{W}=\sqrt{\varepsilon^*}\bar{f}(L/W,\nu), \quad (16)$$

showing the characteristic $\sqrt{\varepsilon^*}$ dependence of the height H. Equation (16) is plotted in Fig. 10(b) for different aspect ratios of the film, indicating that for the aspect ratios analyzed, its effect on H/W is small. This can also be deduced from the inset of Fig. 10(b), clearly showing that the dependence of the slope of Fig. 10(b) on L/W is weak for $L/W>1$. These results are in close agreement with the numerical results shown in Fig. 10(a). Note that the analytical solution and simulation results do not match one-to-one, which may be due to the assumed functional form of the buckled-up profile in the analytical solution [Eq. (10)] which does not exactly represent the profile in the simulations.

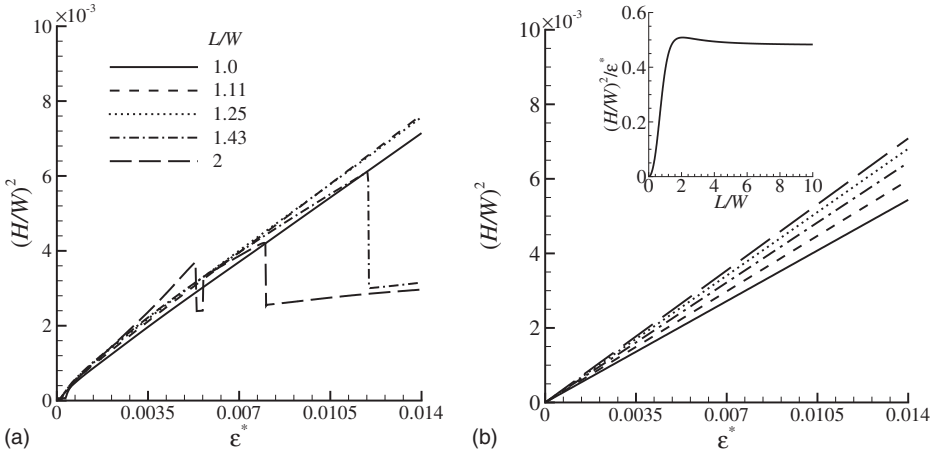

FIG. 10. (a) Simulation results for the normalized buckling amplitude $(H/W)^2$ plotted as a function of eigenstrain for films with different aspect ratio. (b) Analytical solution of normalized buckling amplitude $(H/W)^2$ as a function of eigenstrain (ε^*) for films of different aspect ratio (L/W). Each line type corresponds to a specific aspect ratio of the film as shown in Fig. 10(a). The inset of figure (b) shows the slope of the lines as a function of the aspect ratio.

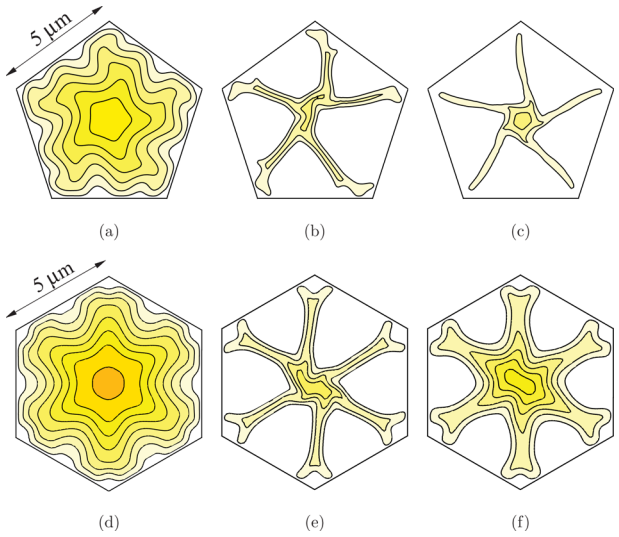

FIG. 11. (Color online) Contour plots of the normalized out-of-plane ($\bar{z}$) deflection during bond-back for pentagonal (a)–(c) and hexagonal (d)–(f) films of side 5 μm and thickness 30 nm. During the bond-back stage the corresponding values of σ_{max}/E are (a) and (d) 0.0 (i.e., the configuration at 2% eigenstrain during buckling up), (b) 1.25×10^{-3}, (c) 1.25×10^{-3} with a higher damping factor than in (b), (e) 0.375×10^{-3}, and (f) with 0.375×10^{-3} with a higher film thickness (50 nm) than in (e). The value of H^* for the above case is 1200 nm (see Fig. 4 for legend).

C. Pentagonal and hexagonal films

Next, we study the patterns formed in films with a pentagonal and hexagonal geometry. Figure 11 shows the contour plots of the out-of-plane deflection for pentagonal (a)–(c) and hexagonal (d)–(f) films with a side length of 5 μm and a thickness of 30 nm during the bond-back stage. The bond back is started from the configuration of the film at 2% eigenstrain similar to the square films. Figures 11(a) and 11(d) show the configuration at the beginning of bond-back (i.e., at 2% eigenstrain) for pentagonal and hexagonal films, respectively. Figure 11(b) shows the bond-back configuration at $\sigma_{max}/E=1.25\times10^{-3}$, i.e., an interface energy of 0.47 J/m^2 (for $\delta_n=20$ nm), while Fig. 11(c) shows the configuration at the same interface energy but with a higher damping factor for pentagonal film of thickness 30 nm.[41] From the figures [Figs. 11(b) and 11(c)] it can be seen that the final pattern configuration with higher damping is more symmetric and has more narrow channels. This is due to the lower kinetic energy in the system during bond-back, which does not create any disturbances to break the symmetry as in the system with lower damping shown in Fig. 11(b). Note that both configurations can be observed in the optical micrographs of the experimental system [see Fig. 1(b)]. It can be observed that the initial configuration of the bond-back stage (i.e., the configuration at the end of 2% eigenstrain during buckling-up process) for hexagonal film [Fig. 11(d)] is still symmetric, in contrast to the pentagonal film in Fig. 11(a). It seems that the level of symmetry of the initial film shape affects the susceptibility to symmetry breaking of the buckling profile. Squares and hexagons (two axes of symmetry) break symmetry at eigenstrains of 1.78% and 2.1%, while pentagons (one axis of symmetry) break symmetry at much smaller eigenstrains (1.1%). Figures 11(e) and 11(f) shows the bond-back configuration at $\sigma_{max}/E=0.375\times10^{-3}$ corresponding to an interface energy of 0.142 J/m^2, while Fig. 11(f) corresponds to a higher thickness ($t=50$ nm). The film with a lower thickness bonds back with less symmetry than the thicker film, while the channels are more narrow. The observation is in correspondence to those of the square films (see Fig. 6). Note that for both thicknesses the buckled-up configurations are identical [conform Fig. 5(b)].

Finally, we investigate the film height H during the buckling-up stage of the pentagonal, hexagonal and square films. Figure 5(b) suggests that the thickness dependence for square films is small. Indeed, by plotting $(H/W)^2$ versus ε^* a very small thickness dependence can be observed, while the curve can be well fitted to $(H/W)^2=0.6\varepsilon^*$. In other words, H^2/A, where $A=W$ is the area of the square film, scales with ε^*. It turns out that such a scaling relation can also be extended to other film geometries as well. Figure 12(a) shows the film height H normalized with an equivalent film width (W_{eq}) plotted as a function of eigenstrain (ε^*). The equivalent film width W_{eq} is the length of the side of a square of the same area as the polygonal film under consideration (i.e., the square root of the film area). Thus $W_{eq}=W$ for square, $W_{eq}=1.31W$ for pentagonal, and $W_{eq}=1.61W$ for hexagonal films. It can be observed that the normalized buckling amplitude is independent of film shape, film size and film thickness when normalized with W_{eq}. The final pattern/morphology after bond back is governed by the interface energy, film thickness, film size and eigenstrain in the film.

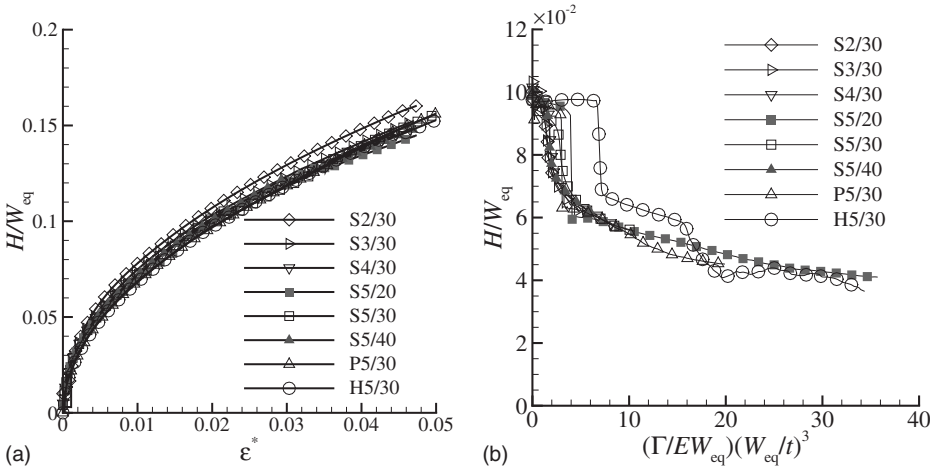

FIG. 12. (a) Normalized buckling amplitude (H/W_{eq}) as a function of eigenstrain (ε^*) (b) Normalized buckling amplitude (H/W_{eq}) as a function of the nondimensional parameter $(\Gamma/EW_{eq})(W_{eq}/t)^3$ for films of square (S), pentagonal (P), and hexagonal (H) geometry. The first number in the legend corresponds to the side length of the film in micrometer and the second number corresponds to the film thickness in nanometer.

This final configuration is determined by the balance between the interface energy in the rebonded region and the strain energy of the film. By neglecting the strain energy due to stretching, Annabattula *et al.*[30,36] have shown that the bond-back process is governed by the nondimensional parameter $(\Gamma/EW)(W/t)^3$, where $\Gamma=\sigma_{max}\delta_n \exp(1)$. However, for polygonal films we replace W by W_{eq} in the above nondimensional parameter. Figure 12(b) shows the evolution of the normalized amplitude (H/W_{eq}) as a function of normalized interface strength $[\Gamma/(EW_{eq})](W_{eq}/t)^3$ during the bond-back stage for square, pentagonal and hexagonal films of different size and thickness. All the curves collapse onto a single curve with some initial scatter, especially for the hexagonal film. The normalized Figs. 12(a) and 12(b) can be seen as master curves for the buckling-up and bond-back behavior for thin films of different shape, size and thickness.

IV. SUMMARY AND CONCLUSIONS

We have developed a finite element model to describe the mechanism of pattern formation as a result of buckling-up followed by bond-back of prestressed thin films on a rigid substrate. We studied films with different size, thickness, and shape, including square, rectangular, pentagonal and hexagonal films. During eigenstrain loading, square films of width W first buckle in their initial (Euler) buckling mode at the critical buckling strain ε_c^*. After an initial symmetric evolution of the deflection profile, the symmetry of the deflection pattern breaks when the wavelength of the wriggles near the fixed boundary starts to decrease. The strain at which wavelength reduction initiates and symmetry breaking commences depends on the normalized thickness t/W. The normalized buckling height H/W, however, is more-or-less independent of thickness and is observed to scale linearly with $\sqrt{\varepsilon^*}$. During bond back the deflection morphology converges to a fourfold ridging pattern having features that show a close resemblance with the experimental film systems of similar size and shape. Rectangular films of large length to width ratio and relatively small thickness go through a transition in buckling shapes from the initial Euler mode, through the varicose mode into the antisymmetric telephone-cord mode. Increasing the thickness postpones the telephone-cord mode to occur at larger strains, while the ridging pattern becomes more regular with a decrease in length to width ratio, converging to the fourfold ridging pattern for square films. We have also performed analytical calculations based on the minimization of strain energy in the film to study the evolution of buckling height H. We found that H/W only depends weakly on normalized film thickness t/W and aspect ratio L/W and we confirmed the linear correlation between H/W and $\sqrt{\varepsilon^*}$.

Finally, we studied the effect of film shape on pattern formation for pentagonal and hexagonal films. We found that the evolution of height H for all film shapes can be captured by one master curve which scales linearly with $\sqrt{\varepsilon^*}$ if normalized by W_{eq}, being the square-root of the film area. In addition, the bond-back mechanism is governed by the eigenstrain value at the end of the buckling-up stage and the dimensionless parameter $[\Gamma/(EW_{eq})](W_{eq}/t)^3$, relating the film dimensions to the interface energy $\Gamma=\sigma_{max}\delta_n \exp(1)$. The Young's modulus of the film does not enter the buckling-up process during the initiation of buckling or during postbuckling. It does enter, however, during bond-back in which it contributes to the competition between the interface energy and the strain energy of the film, ultimately dictating the final wrinkle morphology.

ACKNOWLEDGEMENTS

The authors would like to acknowledge the financial support from MicroNed, The Netherlands under the Project No. FUNMOD-WP-4C-4. The authors would also like to thank Professor W. T. S. Huck (University of Cambridge, UK) and Dr. Y. Mei and Professor O. G. Schmidt (IFW Dresden, Germany) for valuable discussions.

[1] C. Harrison, C. M. Stafford, W. Zhang, and A. Karim, Appl. Phys. Lett. **85**, 4016 (2004).
[2] Y. Xia, E. Kim, X.-M. Zhao, J. A. Rogers, M. Prentiss, and G. M. Whitesides, Science **273**, 347 (1996).
[3] S. Edmondson and W. T. S. Huck, Adv. Mater. **16**, 1327 (2004).
[4] S. Edmondson, K. Frieda, J. E. Comrie, P. R. Onck, and W. T. S. Huck, Adv. Mater. **18**, 724 (2006).
[5] Y. Sun, W. M. Choi, H. Jiang, Y. Y. Huang, and J. A. Rogers, Nat. Nanotechnol. **1**, 201 (2006).
[6] H. Jiang, Y. Sun, J. A. Rogers, and Y. Huang, Appl. Phys. Lett. **90**, 133119 (2007).
[7] A. J. Baca, J.-H. Ahn, Y. Sun, M. A. Meitl, E. Menard, H.-S. Kim, W. M. Choi, D.-H. Kim, Y. Huang, and J. A. Rogers, Angew. Chem., Int. Ed. **47**, 5524 (2008).
[8] D.-H. Kim, J.-H. Ahn, W. M. Choi, H.-S. Kim, T.-H. Kim, J. Song, Y. Y. Huang, Z. Liu, and J. A. Rogers, Science **320**, 507 (2008).
[9] S. P. Lacour, S. Wagner, Z. Huang, and Z. Suo, Appl. Phys. Lett. **82**, 2404 (2003).
[10] Y. Mei, D. J. Thurmer, F. Cavallo, S. Kiravittaya, and O. G. Schmidt, Adv. Mater. **19**, 2124 (2007).
[11] A. Malachias, Y. Mei, R. K. Annabattula, C. Deneke, P. R. Onck, and O. G. Schmidt, ACS Nano **2**, 1715 (2008).
[12] P. Watts and C. Wiles, Chem. Commun. (Cambridge) **2007**, 443.
[13] K. Efimenko, M. Rackaitis, E. Manias, A. Vaziri, L. Mahadevan, and J. Genzer, Nature Mater. **4**, 293 (2005).
[14] R. Langer and J. P. Vacanti, Science **260**, 920 (1993).
[15] K. Efimenko, J. Finlay, M. E. Callow, J. A. Callow, and J. Genzer, ACS Appl. Mater. Interfaces **1**, 1031 (2009).
[16] S. W. Turner, A. M. Perez, A. Lopez, and H. G. Craighead, J. Vac. Sci. Technol. B **16**, 3835 (1998).
[17] M. Foquet, J. Korlach, W. Zipfel, W. W. Webb, and H. G. Craighead, Anal. Chem. **74**, 1415 (2002).
[18] J. Peng, H. Wang, B. Li, and Y. Han, Polymer **45**, 8013 (2004).
[19] E. Schäffer, T. Thurn-Albrecht, T. Russel, and U. Steiner, Nature (London) **403**, 874 (2000).
[20] M. B. Stern, M. W. Gies, and J. E. Curtin, J. Vac. Sci. Technol. B **15**, 2887 (1997).
[21] N. R. Tas, J. W. Berenschot, P. Mela, H. V. Jansen, M. Elwenspoek, and A. van den Berg, Nano Lett. **2**, 1031 (2002).
[22] J. Haneveld, H. Jansen, E. Berenschot, N. Tas, and M. Elwenspoek, J. Micromech. Microeng. **13**, S62 (2003).
[23] J. Haneveld, E. Berenschot, P. Maury, and H. Jansen, J. Micromech. Microeng. **16**, S24 (2006).
[24] H. T. Hoang, I. M. Segers-Nolten, J. W. Berenschot, M. J. de Boer, N. R. Tas, J. Haneveld, and M. Elwenspoek, J. Micromech. Microeng. **19**, 065017 (2009).
[25] N. Bowden, S. Brittain, A. G. Evans, J. W. Hutchinson, and G. M. Whitesides, Nature (London) **393**, 146 (1998).
[26] J. Huang, M. Juszkiewicz, W. H. de Jeu, E. Cerda, T. Emrick, N. Menon, and T. P. Russell, Science **317**, 650 (2007).
[27] E. Cerda, K. Ravi-Chandar, and L. Mahadevan, Nature (London) **419**, 579 (2002).
[28] A. I. Fedorchenko, A.-B. Wang, V. I. Mashanov, and H.-H. Cheng, J. Mech. **21**, 131 (2005).

[29]M.-W. Moon, K.-R. Lee, K. H. Oh, and J. W. Hutchinson, Acta Mater. **52**, 3151 (2004).
[30]R. K. Annabattula, W. T. S. Huck, and P. R. Onck, J. Mech. Phys. Solids **58**, 447 (2010).
[31]F. Bloom and D. Coffin, *Handbook of Thin Plate Buckling and Postbuckling* (Chapman & Hall/CRC, New York, 2001).
[32]X. P. Xu and A. Needleman, Modell. Simul. Mater. Sci. Eng. **1**, 111 (1993).
[33]O. C. Zienkiewicz and R. L. Taylor, *The Finite Element Method: The Basics*, 5th ed. (Butterworth-Heinemann, Oxford, 2000), Vol. 1.
[34]ABAQUS, Analysis user's manual, Version 6.7, Dassault systems, Simulia, Rising Sun Mills 166 Valley Street Providence RI 02909-2499 USA, 2007.
[35]A gap of 20 nm is maintained between the film and the substrate to avoid instabilities in the static solution procedure during the buckling-up stage.
[36]R. K. Annabattula, J. M. Veenstra, Y. Mei, O. G. Schmidt, and P. R. Onck, Phys. Rev. B **81**, 224114 (2010).
[37]K. Sezawa, Aeronautical Research Institute Technical Report No. 69, 1931, p. 45; http://airex.tksc.jaxa.jp/pl/dr/lS4146508000.
[38]G. I. Taylor, ZAMM **13**, 147 (1933).
[39]P. R. Everall and G. W. Hunt, Int. J. Non-Linear Mech. **35**, 1067 (2000).
[40]B. Audoly, Phys. Rev. Lett. **83**, 4124 (1999).
[41]The dissipated energy for the damping factor of Fig. 11(b) is 0.5% of the total energy, while with the higher damping factor of Fig. 11(c) it is 5% of the total energy in the system.